Response of normal faults to glacial-interglacial fluctuations of ice and water masses on Earth's surface

Andrea Hampel[1,2] and Ralf Hetzel[3]

Received 26 October 2005; revised 27 February 2006; accepted 2 March 2006; published 22 June 2006.

[1] Changes in surface loads during glacial-interglacial cycles and the associated flexure and rebound of the lithosphere alter the stress field in actively extending regions and may lead to slip rate variations on normal faults. In particular, loading may cause a period of seismic quiescence that is followed by temporal clustering of earthquakes during and after unloading. Here we present a suite of finite element experiments to evaluate how the magnitude, distribution, and temporal evolution of the load, as well as rheological parameters of the lithosphere and asthenosphere, influence the response of a normal fault. The results show that the duration of the seismically quiet period during loading and the intensity of the slip rate increase during unloading are primarily controlled by the magnitude of the load. The time lag between the changes in loading and the reaction of the fault is mainly determined by the viscosity of the asthenosphere. Parameters that play only a minor role for the fault's response include the rate of load removal, fault strength, and the thickness of the lithosphere. Our results imply that earthquake recurrence models derived from Holocene slip histories may not be representative for the long-term evolution of seismogenic faults.

Citation: Hampel, A., and R. Hetzel (2006), Response of normal faults to glacial-interglacial fluctuations of ice and water masses on Earth's surface, *J. Geophys. Res.*, *111*, B06406, doi:10.1029/2005JB004124.

1. Introduction

[2] The transition between glacial and interglacial periods is associated with considerable changes in the mass distributed on Earth's surface in the form of ice sheets, glaciers and lakes and owing to the rise and fall of the sea level [e.g., *Shackleton*, 1987; *Lambeck and Chappell*, 2001]. During glacial maxima, the load applied to Earth's surface may involve ice masses with a thickness of up to 2000 m (e.g., in the Alps [*Florineth and Schlüchter*, 1998; *Kelly et al.*, 2004]) and lakes of several hundred meters depth (e.g., Lake Bonneville in Utah [*Gilbert*, 1890; *Oviatt et al.*, 1992; *Bartov et al.*, 2002]). Such mass fluctuations affect the lithosphere, which responds by flexure and rebound to the addition and removal of mass on its surface, respectively [e.g., *Gilbert*, 1890; *Walcott*, 1970; *Bills and May*, 1987; *Bills et al.*, 1994; *Cohen*, 1993; *Wu et al.*, 1999; *Sauber et al.*, 2000; *Stewart et al.*, 2000; *Watts*, 2001]. The resulting changes in the stress state of the lithosphere are caused by the process of loading and unloading itself, which primarily affects the vertical stress, and by the induced flexure and rebound, which mainly alters the horizontal stress. As Earth's crust is close to failure in actively deforming regions as well as in intracontinental settings that are often considered as tectonically quiet [*Zoback et al.*, 1989], these changes in the lithospheric state of stress may influence faulting in Earth's crust such that earthquakes are promoted or suppressed. For example, field data from Scandinavia and North America suggest that the melting of the ice sheets was followed by the formation and/or reactivation of faults, as indicated by paleoseismologic evidence for the occurrence of earthquakes and the development of late Pleistocene/early Holocene fault scarps [*Adams et al.*, 1991; *Arvidsson*, 1996; *Stewart et al.*, 2000; *Fjeldskaar et al.*, 2000; *Muir-Wood*, 2000].

[3] The effect of loading and unloading on the style of faulting has previously been analyzed using Mohr diagrams for stress [*Johnston*, 1987, 1989; *Wu and Hasegawa*, 1996a, 1996b; *Sauber and Molnia*, 2004]. The Mohr diagram for stress with the Mohr circle [*Mohr*, 1900] [see, e.g., *Twiss and Moores*, 1992] is an elegant way to illustrate the state of stress at a point (Figure 1). In the diagram, the normal stress σ_n on the horizontal axis is plotted against the shear stress τ on the vertical axis. The Mohr circle has its center on the horizontal axis; its intersections with this axis define the maximum and minimum principal stresses σ_1 and σ_3 (Figure 1). Thus the diameter of the Mohr circle is equal to the magnitude of the differential stress $\sigma_1 - \sigma_3$. Each point on the Mohr circle represents the orientation of a plane in physical space and the normal and shear stresses acting on this plane can be read from the horizontal and vertical axes, respectively (note that compressive stresses are considered positive).

[1] Institute of Geological Sciences, University of Bern, Bern, Switzerland.
[2] Now at Institut für Geologie, Mineralogie und Geophysik, Ruhr-Universität Bochum, Bochum, Germany.
[3] Geologisch-Paläontologisches Institut, Universität Münster, Münster, Germany.

0148-0227/06/2005JB004124$09.00

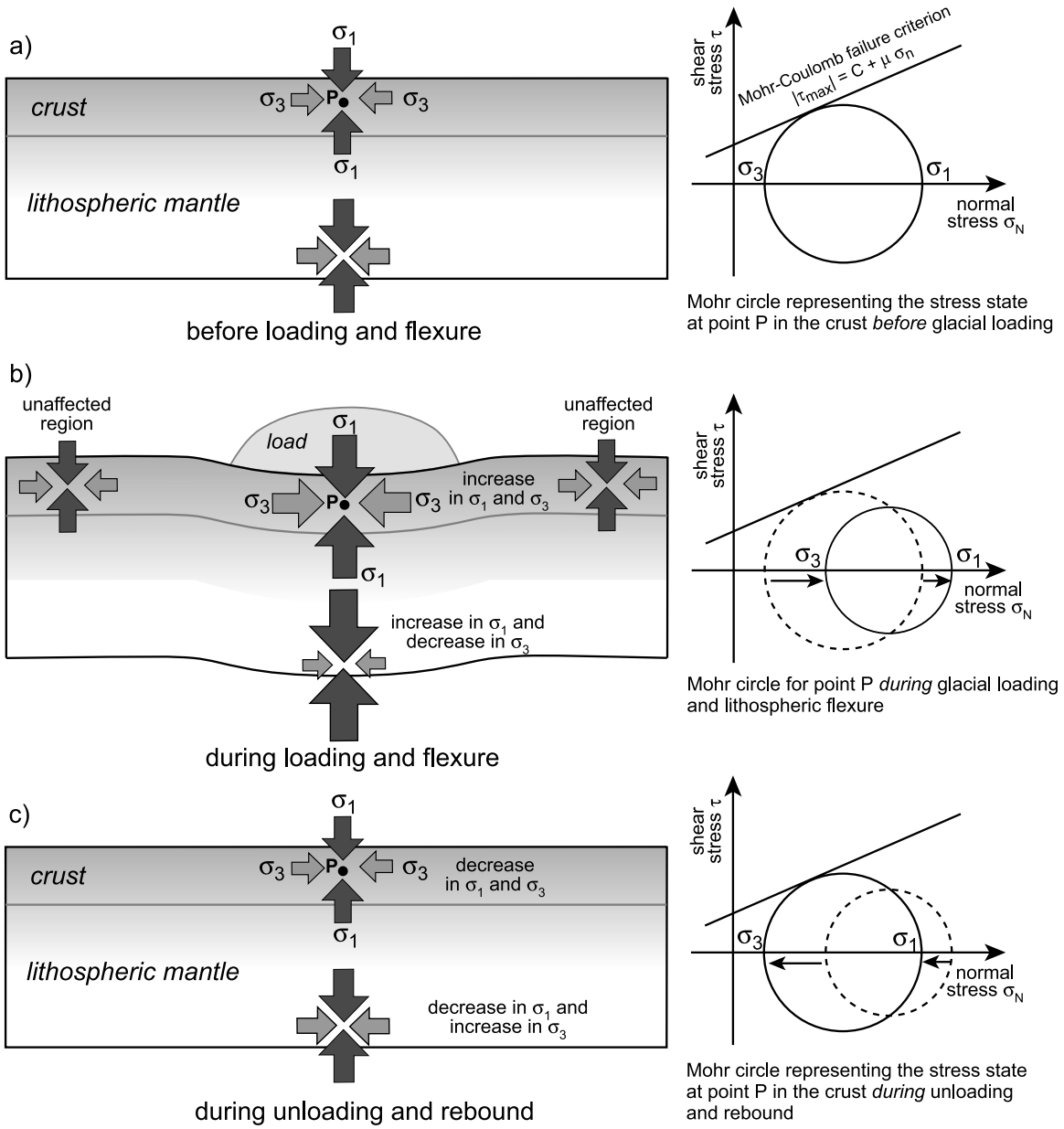

Figure 1. State of stress before, during, and after glacial loading and flexure in a region of active extension, where the maximum principal stress σ_1 is vertical. (a) Before loading, the Mohr circle for stress, which represents the stress state at a point *P,* touches the line representing the Mohr-Coulomb failure criterion; that is, normal faulting occurs (see text for a detailed description of the Mohr diagram and the Mohr-Coulomb failure criterion). (b) Application of a load to Earth's surface increases σ_1. Flexure of the lithosphere, however, affects the horizontal stress, leading to an increase in σ_3 in the upper part of the lithosphere and a decrease in σ_3 in its lower part. At point *P* the overall effect is a reduction of the differential stress $\sigma_1-\sigma_3$; that is, the diameter of the Mohr circle decreases. In other words, upon loading, the Mohr circle becomes smaller and is shifted to the right with the result that normal faulting stops. (c) In the course of unloading and elastic rebound the Mohr circle is shifted to the left, and its diameter increases again such that it touches the line of the Mohr-Coulomb failure criterion; that is, normal faulting starts again. Note that the thickness of the ice sheet is exaggerated with respect to the lithospheric thickness.

[4] On the basis of the analysis of Mohr diagrams for stress, *Johnston* [1987] showed that the absence of earthquakes in today's polar regions, where the vertical principal stress is currently the minimum principal stress σ_3, can be explained by the presence of the large ice sheets in Antarctica and Greenland. The ice sheets increase σ_3 and hence reduce the differential stress $\sigma_1-\sigma_3$, with the result that faulting is suppressed [*Johnston*, 1987]. *Johnston*'s [1987] analysis neglected, however, the effect of flexural stresses. In order to evaluate the stress state resulting from both

loading and unloading as well as from lithospheric flexure and rebound, numerical models have been developed, which also account for the behavior of the sublithospheric mantle [*Johnston et al.*, 1998; *Klemann and Wolf*, 1998; *Wu et al.*, 1999; *Wu and Johnston*, 2000]. Numerical experiments showed that the horizontal stress and the wavelength of the lithospheric flexure depend on the viscosity of the underlying mantle [*Johnston et al.*, 1998]. Furthermore, the general style of faulting was predicted on a continental scale for the Fennoscandian and North American shields, indicating that after deglaciation normal faulting should occur at the paleomargin of the ice sheets, whereas thrust faulting should prevail within the formerly glaciated region [*Johnston et al.*, 1998; *Wu et al.*, 1999]. However, none of these numerical models included discrete faults, with the consequence that the actual rates of faulting could not be predicted.

[5] Recently, the slip history of a normal fault during loading and unloading of an actively extending lithosphere has been modeled by using finite element techniques that allow the incorporation of a discrete fault plane [*Hetzel and Hampel*, 2005]. In contrast to compressive settings, regions of normal faulting, where the maximum principal stress σ_1 is vertical (Figure 1a), should experience an increase in σ_1 during loading and a decrease in σ_1 during unloading. Hence if lithospheric flexure and rebound are neglected, faulting should be enhanced during the glacial period and suppressed after deglaciation. Paleoseismologic data from normal faults that have experienced considerable loading during the last glacial period, however, indicate the opposite behavior [e.g., *Friedrich et al.*, 2003]. As the numerical experiments by *Hetzel and Hampel* [2005] show, this can be explained by the induced flexural stresses that outweigh the loading-induced increase in σ_1 by decreasing σ_3 during loading and increasing σ_3 during unloading (Figures 1b and 1c). Thereby the differential stress is altered such that the fault experiences a phase of seismic quiescence during application of the load and a marked increase in slip rate when the load is removed again. The enhanced slip accumulation that follows the unloading of the crust may be interpreted to compensate the slip deficit, which the fault attained during the period of seismic quiescence, and corresponds to a period with an increased frequency of earthquakes. The variations in the slip rate may occur with a time lag of several thousand years owing to the viscosity of the lithospheric mantle and the asthenosphere [*Hetzel and Hampel*, 2005].

[6] Emanating from this previous work, the present study aims to analyze in more detail the influence of different parameters, like the magnitude and the spatial distribution of the load, the viscosity of the asthenosphere, and the strength of the fault, on the timing and magnitude of the slip rate variations during loading and subsequent unloading. Using the model from *Hetzel and Hampel* [2005] as a reference model, we present a suite of experiments, in which one parameter at a time is varied.

2. Setup and Results of the Reference Model

[7] The reference model consists of a 1000-km-long lithosphere, which is divided into a 30-km-thick, elasto-plastic crust and a 70-km-thick, elasto-visco-plastic lithospheric mantle (Figure 2a). The rheological parameters are given in Figure 2a. Gravity is included in the model as a body force. In order to account for isostasy, a lithostatic pressure and linear spring and dashpot elements are applied to the bottom of the model. The stiffness of the springs and the viscosity of the dashpots are defined to represent an asthenosphere with a density of $\rho = 3200$ kg/m^3 and a viscosity of $\eta = 5 \times 10^{19}$ Pa s, respectively. Such a viscosity value for the asthenosphere is within the range of values determined from the isostatic rebound of Fennoscandia and North America [e.g., *Fjeldskaar*, 1994; *Lambeck et al.*, 1998].

[8] The bottom of the model is free to move in the vertical and the horizontal directions, with exception of the corners that are fixed in the vertical direction. In the center of the model, a discrete fault plane is embedded in the crust as a contact interface between the element surfaces [e.g., *Ellis and Stöckhert*, 2004; *Kaiser et al.*, 2005; *Schwarz and Henk*, 2005]. The fault plane cuts the entire crust and dips at 60°. Such a dip has been inferred for many normal faults from earthquake focal mechanism in actively extending regions [e.g., *Jackson*, 1987]. Slip on the fault is controlled by the Mohr-Coulomb failure criterion $|\tau_{max}| = C + \mu\,\sigma_n$ [*Coulomb*, 1773] [see, e.g., *Jaeger and Cook*, 1979], which relates the critical shear stress τ_{max}, at which slip is initiated, to the normal stress σ_n by the coefficient of friction μ. C is the cohesion. In the Mohr diagram, the Mohr-Coulomb failure criterion plots as a straight line, with the friction coefficient μ defining its slope and the y axis intercept representing the cohesion C (Figure 1). Slip on the fault plane occurs if the Mohr circle of stress touches the line of the Mohr-Coulomb failure criterion. In our reference model we use a friction coefficient of $\mu = 0.4$, a cohesion C of zero and a maximum critical shear stress of $\tau_{max} = 1 \times 10^7$ Pa, which reflects that fault rocks have negligible cohesion and a shear strength between 1 MPa and 50 MPa [e.g., *Twiss and Moores*, 1992; *Weijermars*, 1997].

Figure 2. (a) Setup of the reference model. The rheological parameters are density (ρ), elastic modulus (E), Poisson's ratio (υ), plastic yield stress (σ_y), viscosity (η), acceleration due to gravity (g), load (L), velocity (v), and lithostatic pressure (P_{litho}). The lithosphere is extended with a velocity of $v = 1$ mm yr^{-1} on both sides. Slip on the normal fault is controlled by a Mohr-Coulomb failure criterion (τ_{max}: critical shear stress of the fault; μ: coefficient of friction). (b) Results of the reference model [*Hetzel and Hampel*, 2005]. Before loading, the fault slips at a constant rate of 0.2 mm yr^{-1}. The loading function is indicated in black as inset: Slip accumulation stops during loading but is considerably enhanced during unloading. Note that the model time starts from zero at the beginning of the loading function. (c) Evolution of the differential stress for point P located close to the fault at a depth of 12 km. The location of point P is marked in Figure 2d (panel A). (d) Vertical displacement field of the whole model domain at different stages (A–F, as marked in Figure 2b). The displacement is given relative to the model state at 1 Myr model years, i.e., at the beginning of loading. Height of the box in A not to scale to the thickness of the ice sheet. Figures 2a and 2b modified after *Hetzel and Hampel* [2005].

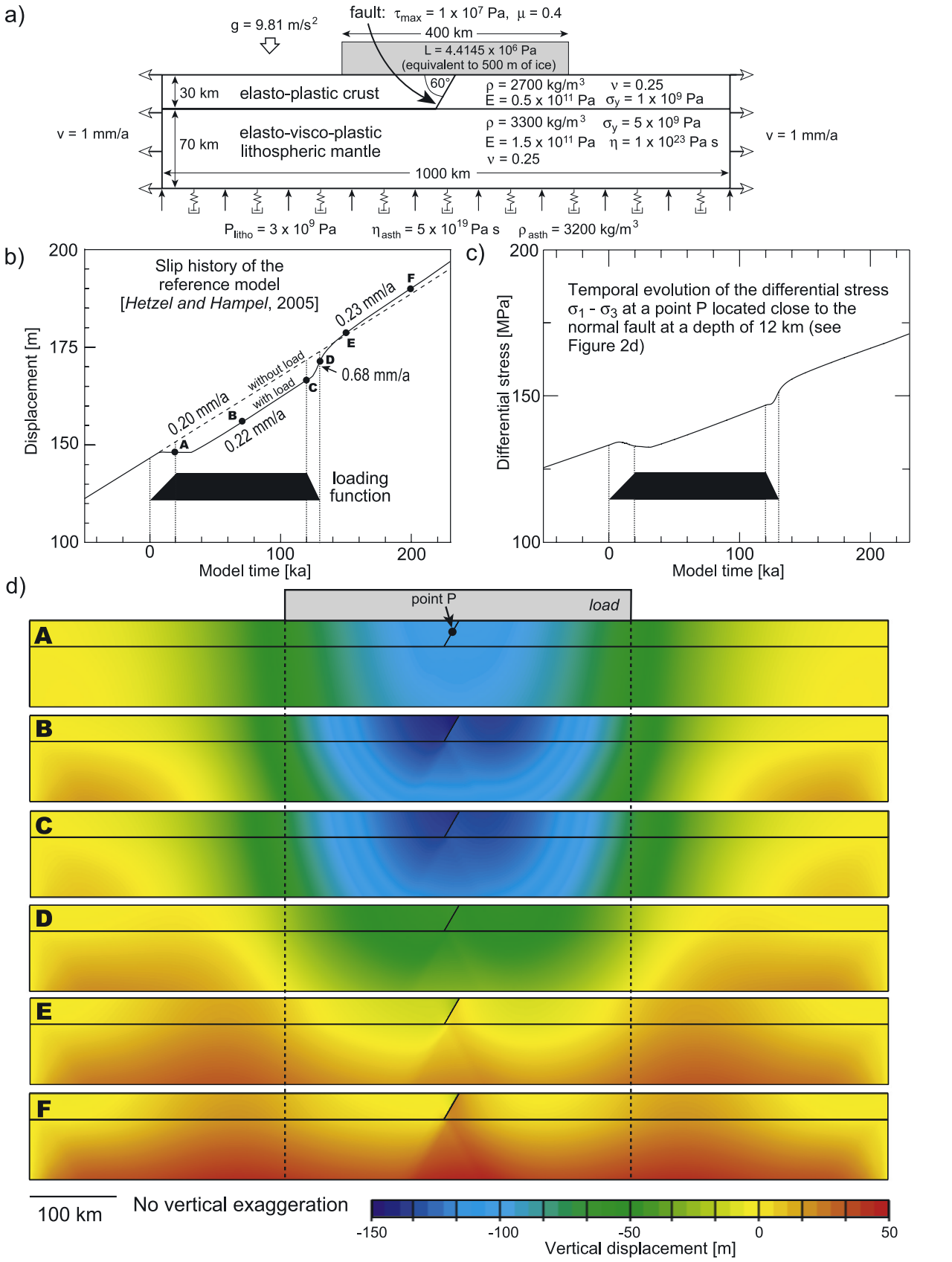
a)
g = 9.81 m/s²
fault: τmax = 1 x 10⁷ Pa, μ = 0.4
400 km
L = 4.4145 x 10⁶ Pa
(equivalent to 500 m of ice)
60°
30 km
elasto-plastic crust
ρ = 2700 kg/m³ ν = 0.25
E = 0.5 x 10¹¹ Pa σy = 1 x 10⁹ Pa
v = 1 mm/a
70 km
elasto-visco-plastic
lithospheric mantle
ρ = 3300 kg/m³ σy = 5 x 10⁹ Pa
E = 1.5 x 10¹¹ Pa η = 1 x 10²³ Pa s
ν = 0.25
v = 1 mm/a
1000 km
Plitho = 3 x 10⁹ Pa
ηasth = 5 x 10¹⁹ Pa s
ρasth = 3200 kg/m³
b)
Slip history of the
reference model
[Hetzel and Hampel, 2005]
Displacement [m]
Model time [ka]
0.20 mm/a
0.22 mm/a
0.23 mm/a
0.68 mm/a
without load
with load
loading
function
A
B
C
D
E
F
c)
Temporal evolution of the differential stress
σ1 - σ3 at a point P located close to the
normal fault at a depth of 12 km (see
Figure 2d)
Differential stress [MPa]
Model time [ka]
d)
point P
load
A
B
C
D
E
F
100 km
No vertical exaggeration
-150
-100
-50
0
50
Vertical displacement [m]

Figure 2

[9] The experiments have been performed with the finite element software ABAQUS [*Hibbitt et al.*, 2002]. The average length of an element's edge is 5 km in the mesh of the crust and 10 km in the mesh of the lithospheric mantle. At the beginning of each model run, the lithosphere is allowed to reach isostatic equilibrium. Throughout the model run, the lithosphere is extended with a horizontal velocity of $v = 1$ mm yr^{-1} on both sides, which are fixed in the vertical direction. Imposing horizontal extension on the sides of the model leads to a stress field with the maximum principal stress σ_1 being vertical and thus to initiation of normal faulting as soon as the critical shear stress is reached on the fault plane. After one million years of model time, a load equivalent to 500 m of ice ($\rho = 900$ kg/m^3) or 450 m of water is applied to the top of the model. The total width of the load, which is distributed symmetrically with respect to the fault, is 400 km (Figure 2a). The temporal evolution of the load's magnitude is described by a loading function: In the reference model, the full magnitude of the load is reached within 20 kyr and then maintained for 100 kyr before a linear decline to zero within 10 kyr (Figure 2b).

[10] Figures 2b–2d show the results of the reference model. The fault slips at a rate of 0.2 mm yr^{-1} for ~1 Myr before the load is applied (Figure 2b); that is, ~10% of the total extension rate of 2 mm yr^{-1} is accommodated by the fault, whereas the remaining strain is distributed over the rest of the model. The ratio between the strain taken up by the fault and the strain distributed over the other parts of the model varies with model length; that is, in a longer model the fault accommodates less strain and slips at a lower rate (not shown). This is because the finite strain (and also the strain rate) decreases with increasing model length if the extension rate, applied at the model boundaries, and the total model time are held constant. As we do not intend to model a specific natural fault with a certain slip rate, the total displacement at the end of a model run is of minor importance for the implications of our study, because the characteristic phases of seismic quiescence and a pronounced slip rate increase (described in detail below) are not a function of the model length.

[11] During a model run, the plastic failure stress σ_y is not reached in the crust nor in the lithospheric mantle; the distributed deformation occurs by elastic strain in the crust and by viscoelastic deformation in the lithospheric mantle. Therefore the model does not show plastic yielding, which would indicate the formation of additional faults in nature during ongoing extension. The predefined model fault, however, reaches a steady state soon after slip is initiated, which is reflected by the constant slip rate before loading (Figure 2b).

[12] The slip history of the reference model shows that after onset of loading slip accumulation on the fault continues for ~7.5 kyr but then ceases for 24.5 kyr (Figure 2b). After this phase of tectonic quiescence the slip rate increases to 0.22 mm yr^{-1}. Unloading starts 100 kyr after the load has reached its full magnitude and leads to a marked increase in the slip rate (0.68 mm yr^{-1}). Within 10 kyr after unloading is completed, the slip rate gradually decreases to a rate of 0.23 mm yr^{-1} (Figure 2b). These changes in slip rate are caused by changes in the differential stress, which decreases during application of the load and increases during removal of the load (Figure 2c). Figure 2d shows the vertical displacement field of the whole model domain at different stages to illustrate the evolution of the model during one glacial-interglacial cycle. Application of the load leads to 100–150 m of subsidence in the center of the model. With the onset of unloading, the footwall and hanging wall of the fault are rapidly uplifted, with the footwall rising at a higher rate than the hanging wall. It is during this phase of rapid rebound that the slip rate of the fault is enhanced by a factor of ~3 to a rate of 0.68 mm yr^{-1} (Figure 2b). After unloading, two main zones of uplift develop at a distance of 50–100 km from the margins of the former load (Figure 2d, panels E and F). An additional experiment with a 2000-km-long model (not shown) reveals that the position and amplitude of these uplift features are not influenced by the horizontal distance between the load and the model boundaries.

[13] The application and removal of the surface load induces rapid changes in the differential stress both in the crust (Figure 2c) and the lithospheric mantle (Figure 3). Owing to viscous flow the lithospheric mantle, these changes in the differential stress are followed by a prolonged phase of stress relaxation (Figure 3).

3. Results of the Parameter Study

[14] In the following, the influence of the different parameters will be analyzed on the basis of experiments, in which one of the model parameters is varied systematically. In the first set of experiments, the properties of the load are varied (Figure 4), whereas the second set of models analyzes the influence of the strength of the fault, the thickness of the lithosphere, and the viscosity of the asthenosphere (Figure 5). Note that in both Figures 4 and 5, all slip histories are shown with the model time starting from zero at the beginning of the loading function. For comparison, the slip history of the reference model and of a model run without loading are shown in all diagrams.

3.1. Magnitude, Spatial Distribution, and Timing of Loading and Unloading

[15] In the first experiments, the magnitude of the load is varied such that it represents 100, 250, 500, 1000, and 2000 m of ice, which is distributed symmetrically with respect to the fault over a width of 400 km (Figure 4a). For loads with an ice thickness larger than 100 m, slip accumulation on the fault stops during loading, whereas it is enhanced during unloading (Figure 4a). An increase in the magnitude of the load leads to a prolongation of the seismically quiet phase and to a more pronounced slip rate increase (Figure 4a). For example, in the model with 250 m of ice, slip ceases for 8.5 kyr, and the slip rate integrated over 5 kyr from the onset of the acceleration is 0.25 mm yr^{-1}. In contrast, fault motion stops for 102.5 kyr in the model with 2000 m of ice and is increased to 1.61 mm yr^{-1} during unloading.

[16] In nature, the load in form of ice and/or water may be applied over distances of 50 km to 500 km and more and may further be distributed asymmetrically with respect to the fault, i.e., restricted to the footwall or the hanging wall. In order to investigate the influence of the width of a symmetrically distributed load, experiments were calculated, in which the width of the load is varied between 500 km and 100 km (Figure 4b). In each of these models the thickness of the load was adjusted such that the weight of

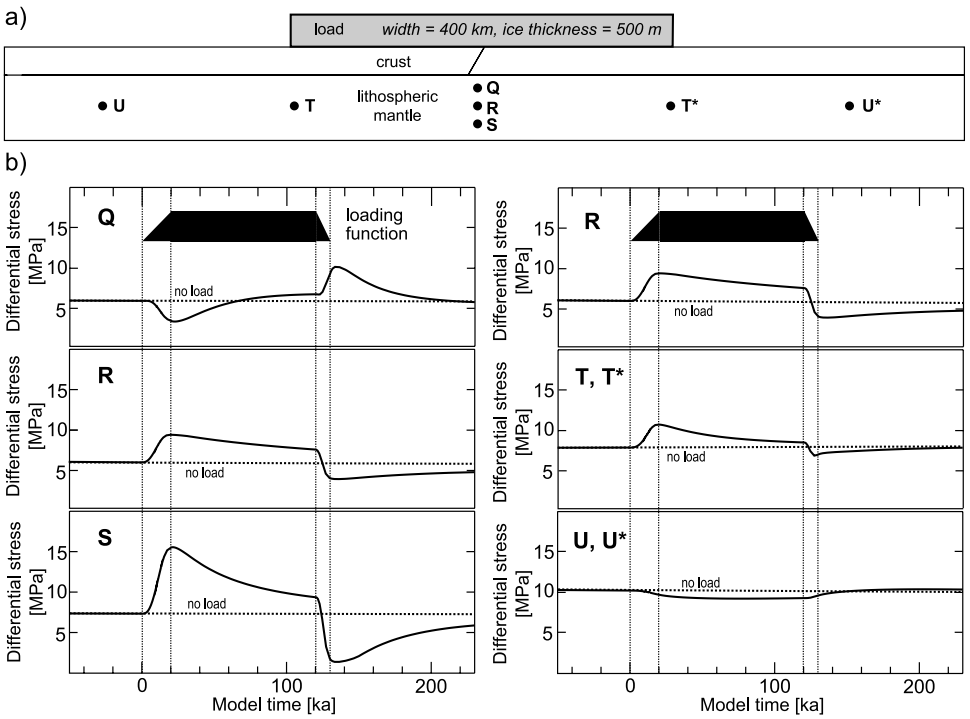

Figure 3. Temporal evolution of the differential stress $\sigma_1-\sigma_3$ at different points in the lithospheric mantle of the reference model. (a) Location of the points in the model. Points *Q*, *R*, and *S* are located below the fault at depths of 39 km, 65 km, and 83 km, respectively. Points *T*, *T**, *U*, and *U** are located at the same depth as point *R*, i.e., at 65-km depth. (b) Temporal evolution of the differential stress for all points (solid curves). Dotted curves show the evolution of the differential stress at the same points without loading and unloading. The diagrams show that both application and removal of the load induces rapid changes in the differential stress. Owing to viscous deformation in the lithospheric mantle, these changes are followed by phases of stress relaxation. The different stress histories reflect that flexure of the lithosphere due to loading increases the horizontal stress σ_3 in the upper part of the lithosphere, whereas σ_3 decreases in the lower part (see Figure 1b). During unloading and rebound, σ_3 decreases in the upper part and increases in the lower part of the model (see Figure 1c). Thus point *Q* experiences a decrease in the differential stress during loading and an increase during unloading. In contrast, the differential stress at points *R*, *S*, *T*, and *T** located in the lower part of the model increases with loading and decreases during unloading. In the outer part of the model (points *U* and *U**) the differential stress is barely affected by the loading history.

the load is the same as in the reference model for all widths. The results show that a decreasing width of the load causes an increase in the length of the period of seismic quiescence. Also, the slip rate increase during unloading is more pronounced. For narrow loads of 100 km and 200 km width the slip rate remains considerably higher than the slip rate of the model without loading but the fault does not accumulate the same amount of displacement (Figure 4b). This means that the slip deficit acquired during the loading phase is not fully compensated by the slip rate increase.

[17] In the next series of experiments, the load is applied asymmetrically with respect to the fault. Figure 4c shows the slip histories resulting from the application of a 200-km-wide and 500-m-thick load to the footwall and hanging wall, respectively. For comparison, the results for the symmetrically distributed, 400-km-wide load with a thickness of 250 m and 500 m are also plotted. In case of footwall loading, the slip history shows the typical sequence of seismic quiescence during loading and slip acceleration during unloading. In case of hanging wall loading, however, the slip rate is first slightly increased whereas unloading stops slip accumulation for nearly 10 kyr (Figure 4c).

[18] As the advance and retreat of glaciers and lakes may occur over different time spans depending on regional

Figure 4. Diagrams with fault displacement plotted versus model time. The diagrams show the slip history of the normal fault under variable magnitude, spatial distribution, and timing of loading and unloading. The temporal evolution of the load is schematically shown in black. Parameters varied are (a) the magnitude of the load, (b) the width of a symmetrically distributed load with a constant weight, (c) the asymmetric distribution of the load, (d) the time, during which the load is at full magnitude, and (e) the rate of load removal. (f) Enlargement of inset in Figure 4e. Note that all slip histories are shown with the model time starting from zero at the beginning of the loading function. For comparison, the slip history of the reference model (thick black curve) and of a model run without loading (dashed line) are shown in all diagrams.

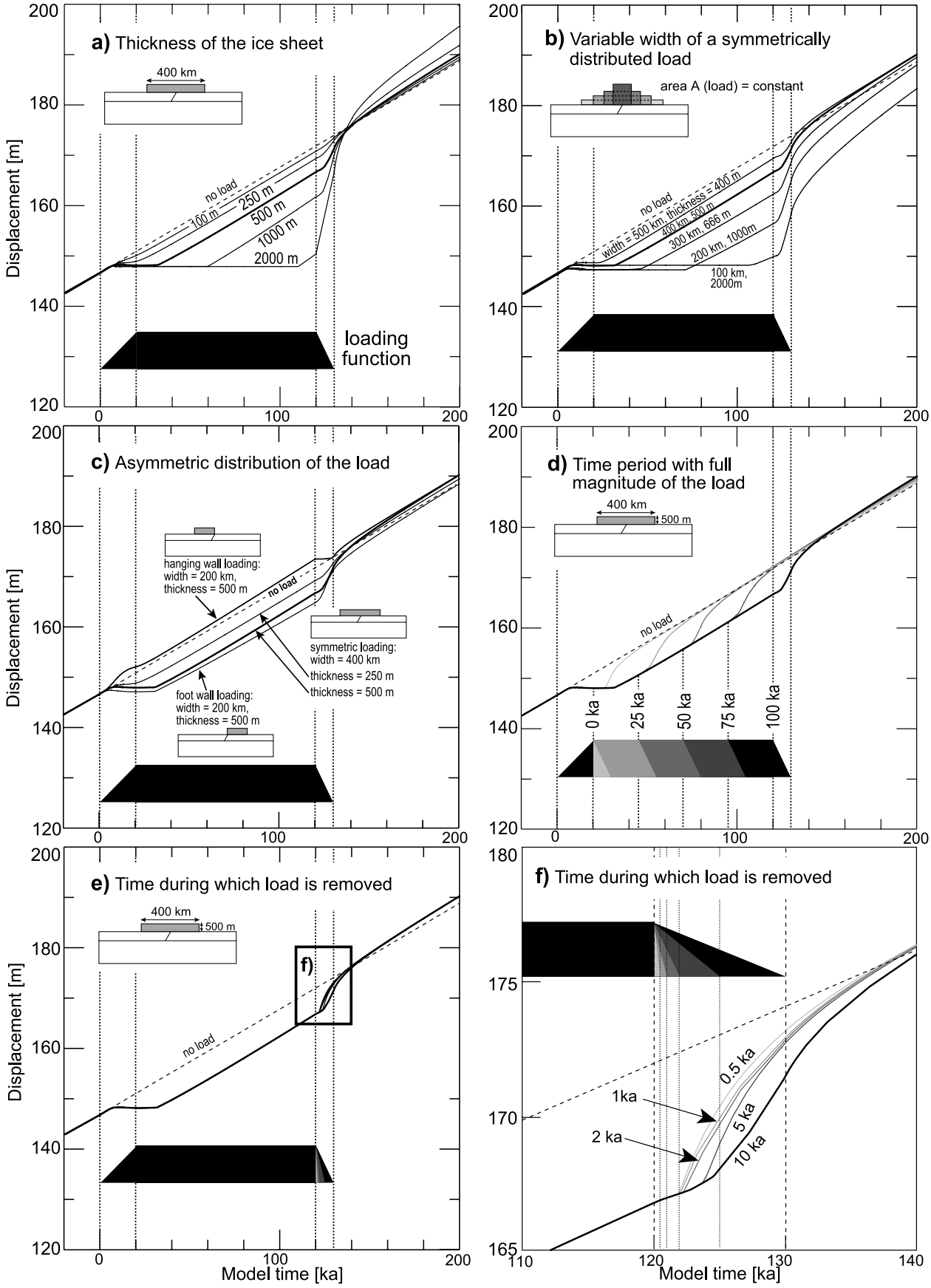
a) Thickness of the ice sheet
400 km
no load
100 m
250 m
500 m
1000 m
2000 m
loading function
Displacement [m]
b) Variable width of a symmetrically distributed load
area A (load) = constant
no load
width = 500 km, thickness = 400 m
400 km, 500 m
300 km, 666 m
200 km, 1000m
100 km, 2000m
c) Asymmetric distribution of the load
hanging wall loading: width = 200 km, thickness = 500 m
no load
symmetric loading: width = 400 km
thickness = 250 m
thickness = 500 m
foot wall loading: width = 200 km, thickness = 500 m
d) Time period with full magnitude of the load
400 km
500 m
no load
0 ka
25 ka
50 ka
75 ka
100 ka
e) Time during which load is removed
400 km
500 m
f)
no load
f) Time during which load is removed
0.5 ka
1ka
2 ka
5 ka
10 ka
Model time [ka]
Model time [ka]

Figure 4

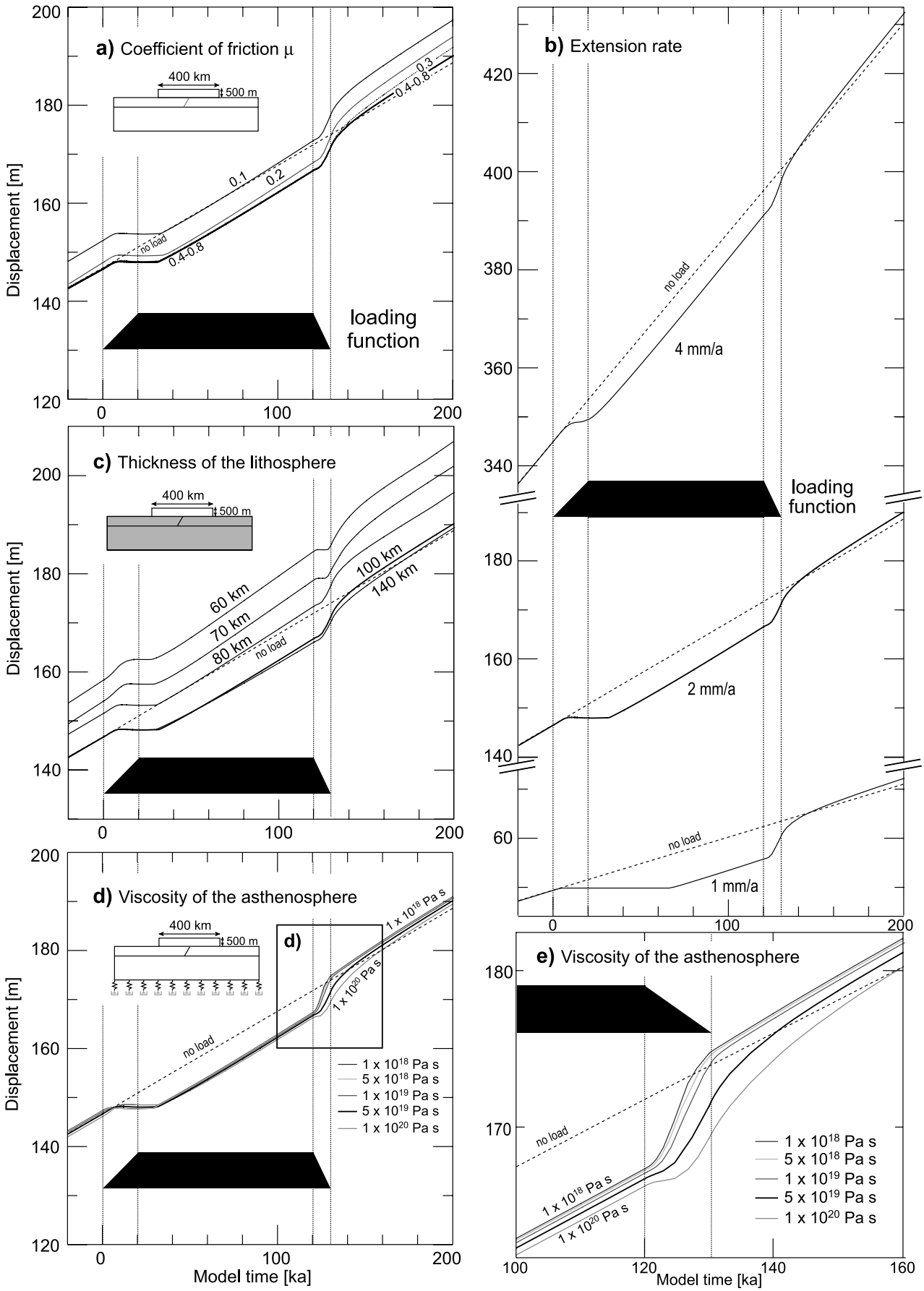
a) Coefficient of friction μ
400 km
500 m
0.1
0.2
0.3
0.4-0.8
no load
0.4-0.8
loading function
Displacement [m]
b) Extension rate
no load
4 mm/a
loading function
2 mm/a
no load
1 mm/a
c) Thickness of the lithosphere
60 km
70 km
80 km
100 km
140 km
no load
d) Viscosity of the asthenosphere
1 x 10^18 Pa s
1 x 10^20 Pa s
no load
1 x 10^18 Pa s
5 x 10^18 Pa s
1 x 10^19 Pa s
5 x 10^19 Pa s
1 x 10^20 Pa s
e) Viscosity of the asthenosphere
no load
1 x 10^18 Pa s
1 x 10^20 Pa s
Model time [ka]

Figure 5

climate conditions [e.g., *Gillespie and Molnar*, 1995], the two following series of experiments investigate how different loading functions affect fault behavior. First, the time span, during which the load is at its full magnitude, is decreased in 25 kyr time steps from 100 kyr to 0 kyr (Figure 4d). If the magnitude of the load starts to decline again immediately after reaching its full magnitude (0 kyr), the slip rate increase is slightly higher than in the reference model (Figure 4d). In all other cases, the slip rate increase equals the one in the reference model; that is, whether the load has been present for 25 kyr or 100 kyr has no effect on fault behavior during postglacial unloading.

[19] Figures 4e and 4f show the displacement time plots from models in which the time span during which the load is removed is reduced from 10 kyr to 0.5 kyr. An increased rate of unloading leads to an earlier onset of slip acceleration in comparison to the reference model (Figure 4f). The slip rate increase is, however, similar in all experiments suggesting that, if the surface load is removed within a few thousand years, the slip rate increase is nearly independent of the rate of mass removal.

3.2. Influence of Fault Strength, Extension Rate, Lithospheric Thickness, and the Viscosity of the Asthenosphere

[20] It is generally expected that the slip rate of the fault depends on its strength, which is reflected by the slope of the Mohr-Coulomb failure criterion in the Mohr diagram and expressed in terms of the coefficient of friction μ. In the next experiments, the friction coefficient μ for the model fault has been varied between 0.1 and 0.8 (Figure 5a). The minor differences between these experiments show that for a lower friction coefficient the displacement accumulated at any stage of the experiment, i.e., before loading, in presence of the load, and after removal of the load, is slightly higher. For example, after a total model time of 1200 kyr (including the time of 1 Myr before loading), the fault with $\mu = 0.1$ has accumulated 197 m of slip in contrast to 190 m of slip in the model with $\mu = 0.8$ (Figure 5a). For friction coefficients of $\mu \geq 0.4$, the differences in the accumulated displacements are negligible. The curves of all experiments are nearly parallel until complete removal of the load, indicating that the acceleration of fault slip during unloading is similar for all experiments (Figure 5a). Only after unloading, the slip rate for lower friction coefficients is again slightly higher as shown by the slight divergence of the curves to the right.

[21] In order to test the effect of the applied extension rate on the temporal evolution of the fault slip rate we performed model runs with extension rates of 1, 2, and 4 mm yr^{-1} (Figure 5b). These experiments reveal that the basic pattern in the slip history of the fault does not change with the extension rate; that is, fault movement stops during loading and accelerates during unloading. The period of seismic quiescence during and after loading depends, however, on the magnitude of the applied extension rate. For a lower extension rate, i.e., 1 mm yr^{-1}, fault slip ceases for a longer period of time following the application of the load, because it takes more time until the ongoing extension of the model decreases the loading-induced horizontal stress to such an extent that the fault starts to slip again. For a higher extension rate, this time period becomes shorter. None of the three experiments with variable extension rate reveals a change in the faulting regime; that is, the largest principal stress σ_1 is always vertical and only normal slip occurs on the fault plane.

[22] The effect of glacial surface loads on lithospheric deformation has been most widely investigated for the tectonically stable Fennoscandian and North American shields, which have lithospheres of more than 100-km thickness [*Johnston et al.*, 1998; *Klemann and Wolf*, 1998, 1999; *Wu et al.*, 1999; *Wu and Johnston*, 2000]. However, considerable loading during the last glacial period also occurred in tectonically active regions, for example in the eastern Basin and Range Province [e.g., *Osborn and Bevis*, 2001], which is characterized by a thinner lithosphere [e.g., *Smith et al.*, 1989; *Zandt et al.*, 1995]. In order to analyze the effect of lithospheric thickness on the slip history of the model fault, it has been varied between 60 km and 140 km by changing the thickness of the lithospheric mantle, while keeping the thickness of the crust constant at 30 km (Figure 5c). The same pattern as in the previous models can be recognized in these experiments. However, slip accumulation generally stops later if the fault is embedded in a thinner lithosphere (Figure 5c). In the two models with a lithospheric thickness of 60 km and 70 km, respectively, there is a second phase of seismic quiescence between the onset of unloading and the rebound-induced acceleration of fault slip. Interestingly, the fault accumulates slightly more displacement if it is embedded in a thinner lithosphere.

[23] The wavelength and timing of postglacial rebound have long been known to depend on the viscosity of the sublithospheric mantle [*Gilbert*, 1890; *Walcott*, 1970; *Bills and May*, 1987; *Bills et al.*, 1994; *Johnston et al.*, 1998; *Klemann and Wolf*, 1998, 1999; *Lambeck et al.*, 1998; *Wu et al.*, 1999; *Wu and Johnston*, 2000; *Watts*, 2001]. Therefore the viscosity of the asthenosphere is expected to have a profound influence on the stress field of the lithosphere and hence on the faults embedded in it. In the last series of experiments, the dashpots at the bottom of the model, which represent the asthenosphere, have been assigned viscosities ranging from 1×10^{18} Pa s to 1×10^{20} Pa s (Figures 5d and 5e). The results reveal that the viscosity of the asthenosphere exerts a fundamental control on the time lag by which the fault responds to a change in the loading function. The higher the viscosity of the asthenosphere, the longer is the time lag with which the fault responds. Furthermore, the viscosity of the asthenosphere strongly influences the

Figure 5. Slip history of the normal fault derived from experiments in which the following parameters have been varied: (a) friction coefficient of the fault, (b) rate of extension applied to both sides of the model, (c) thickness of the lithosphere, and (d) viscosity of the asthenosphere. (e) Blowup of the part of the curves marked by inset in Figure 5d. Note that all slip histories are shown with the model time starting from zero at the beginning of the loading function. For comparison, the slip history of the reference model (thick black curve) and of a model run without loading (dashed line) are shown in all diagrams.

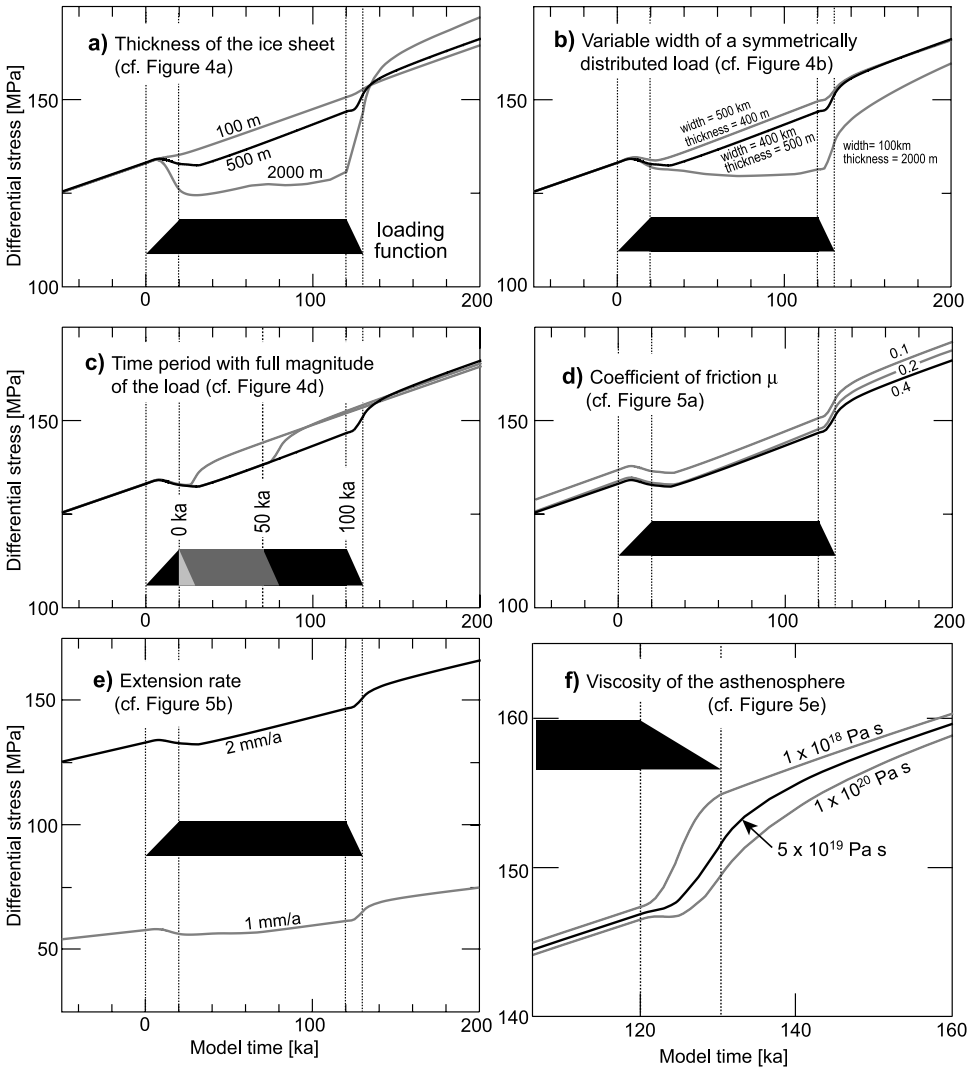

Figure 6. Temporal evolution of the differential stress $\sigma_1-\sigma_3$ for selected experiments from Figures 4 and 5. The differential stress is shown for a point *P* located close to the fault at a depth of 12 km (see also Figure 2d). The diagrams show the evolution of the differential stress in the reference model (black curve) and the experiments in which the following parameters were varied (gray curves): (a) Thickness of the ice sheet, (b) width of a symmetrically distributed load, (c) time period with full magnitude of the load, (d) coefficient of friction of the fault, (e) extension rate, and (f) viscosity of the asthenosphere.

intensity and duration of the slip rate increase that follows the removal of the load. A less viscous asthenosphere leads to a higher slip rate increase and *vice versa*. The higher the viscosity of the asthenosphere, the longer is the time period during which the fault motion is enhanced.

4. Discussion

4.1. Discussion of Results

[24] We have evaluated the response of a normal fault in an actively extending lithosphere to application and subsequent removal of different loads on a 100-kyr timescale. In nature, such a load may be an ice sheet, glaciers and/or lakes, which vary in size according to temporal changes in climate. All experiments reveal a common basic pattern in the fault's slip history, with periods of seismic quiescence and accelerated fault slip that generally correspond to the phases of loading and unloading, respectively (Figures 4 and 5). An exception occurs if the loading is restricted to the hanging wall, which first induces a cessation of slip during unloading followed by acceleration of fault slip (Figure 4c). This fault behavior, which is somewhat similar to models run *without* lithospheric rebound [*Hetzel and Hampel*, 2005], may indicate that the loading/unloading of the hanging wall has a stronger effect on the stress field in the vicinity of the fault than lithospheric rebound because the fault is located at the margin of the load.

[25] The basic pattern of the temporal evolution of the slip rate during one glacial cycle is modified, to different degrees, by parameters characterizing either the load or the rheology of the lithosphere and asthenosphere. Of the investigated parameters, the magnitude and spatial distribution of the load as well as the viscosity of the asthenosphere exert the strongest control on the temporal evolution of the

fault's response. In contrast, the friction coefficient of the fault or the rate of load removal have only a minor influence on the slip rate variations.

[26] The slip rate variations observed in the experiments are caused by temporal changes in the differential stress $\sigma_1 - \sigma_3$. For the reference model and selected experiments, the evolution of the differential stress at a point *P* located close to the fault at a depth of 12 km is shown in Figure 6. A comparison of these diagrams with the slip histories shown in Figure 4 reveals that the duration of the seismically quiet period is directly related to the time during which the differential stress decreases to a lower level (e.g., Figures 4a, 4b, 6a, and 6b). The magnitude of the slip rate increase during unloading is controlled by the increase in differential stress, which is induced by the rebound of the lithosphere (Figure 1c). The relationship between differential stress and slip rate increase is most clearly revealed in the experiments with a variable viscosity of the asthenosphere (Figures 5e and 6f). A lower viscosity of the asthenosphere causes a faster rebound and a more rapid increase in the differential stress and leads therefore to a more pronounced slip rate increase. Even subtle differences in the temporal evolution of the differential stress are reflected in the slip rate history of the fault. For example, the slightly more pronounced slip rate increase in the experiment, in which unloading starts immediately after the load has reached its full magnitude (Figure 4d), results from a slightly faster increase in the differential stress as compared to the reference model (Figure 6c).

[27] Our two-dimensional model setup does not take into account potential three-dimensional variations in the load or the structure of the lithosphere. *Wu and Hasegawa* [1996b], for example, used three-dimensional models to calculate the stress changes induced by a spatially and temporarily variable load and found that the stress variations may be large enough to cause changes in the style of faulting in regions with little tectonic activity. In contrast to our approach, *Wu and Hasegawa* [1996b] did not include faults in their model, which prohibited the calculation of fault slip rates. If the experimental results are to be compared with natural fault slip rates derived from paleoseismology, the incorporation of faults is, however, essential. Future models on the response of faults will need to incorporate both, three-dimensional variations of the load and discrete fault planes. Constraints about the spatial and temporal evolution of loads will be an essential input for these numerical models.

4.2. Comparison with Slip Histories of Natural Faults

[28] Our model predictions may be compared with the paleoseismologic record of normal faults that have experienced considerable loading during the last glacial period. We note, however, that we do not try to derive specific parameter values from our experiments that might be applicable to the natural faults discussed below, because this would require specific adjustments of the model setup with respect to the load, the structure of the lithosphere and the properties of the asthenosphere. Instead, we would like to draw the attention to the possible relationship between documented slip rate variations for faults and the glacial loading history of these regions.

[29] The basic slip rate pattern that we observe in the model is best documented for the Wasatch Fault, Utah [*Machette et al.*, 1991; *McCalpin and Nishenko*, 1996; *Friedrich et al.*, 2003]. The hanging wall of the Wasatch Fault, which marks the boundary between the Basin and Range Province in the west and the Colorado Plateau and Rocky Mountains in the east, was covered by the huge late Pleistocene Lake Bonneville [*Oviatt et al.*, 1992], whereas the footwall was loaded by glaciers in the Wasatch and Uinta Mountains [*Atwood*, 1909; *Madsen and Currey*, 1979; *Osborn and Bevis*, 2001]. During the largest extent of the lake and glaciers the fault was seismically quiet. After shrinkage of the lake and deglaciation, slip accumulation on the fault accelerated dramatically, as indicated by the occurrence of a cluster of earthquakes since the late Pleistocene/Holocene transition [*Friedrich et al.*, 2003, and references therein]. Using a model with a loading function adjusted to the lake level curve of Lake Bonneville, *Hetzel and Hampel* [2005] showed that the shrinkage of the lake and deglaciation of adjacent mountain ranges provide a feasible mechanism for the slip rate increase of the Wasatch fault. The main parameters controlling the magnitude of the slip rate variations in case of the Wasatch fault should be the large dimensions of Lake Bonneville [*Oviatt et al.*, 1992], the thin lithosphere of the Basin and Range [*Smith et al.*, 1989] and the rather low viscosity of the asthenosphere [*Bills and May*, 1987; *Bills et al.*, 1994].

[30] Another example is provided by a normal fault in the southern Upper Rhine Graben, which has been related to the Basel earthquake in 1356, the largest historical seismic event in central Europe. Paleoseismologic investigations suggest that five earthquakes with a cumulative slip of $\sim$3 m occurred on this fault during the last 13 kyr, which is equivalent to a vertical displacement rate of 0.27 mm yr^{-1} [*Ferry et al.*, 2005]. This rate is by a factor of three higher than the long-term average rate of 0.11 mm yr^{-1} over the last 0.7 Myr [*Ferry et al.*, 2005]. The increased postglacial slip accumulation of the fault may be related to unloading of the lithosphere in the vicinity of the southern Upper Rhine Graben, which was caused by the melting of glaciers in the southern Black Forest, Germany, and the southern Vosges, France [*Zienert*, 1973; *Rahm*, 1977, 1987; *Seret et al.*, 1990]. Similarly, a multiarchive paleoseismologic record of the Swiss Alps indicates a higher level of seismicity after the Last Glacial Maximum, although the type of faulting is in most cases unknown [*Becker et al.*, 2005, and references therein]. Given that the Swiss Alps were covered by up to 2-km thick ice [*Florineth and Schlüchter*, 1998; *Kelly et al.*, 2004] and still experience uplift at least partly caused by postglacial rebound [*Gudmundson*, 1994], we speculate, on the basis of our model results, that the melting of the ice after the Last Glacial Maximum triggered the late Pleistocene increase in earthquake frequency.

[31] Our present study focuses on the response of *normal* faults to postglacial unloading. Field data suggest that a correlation between climate-induced mass fluctuations and increased seismicity may also exist for thrust faults [e.g., *Stewart et al.*, 2000]. In northern Scandinavia, a number of postglacial thrust faults with a length of 50–150 km have been identified [*Stewart et al.*, 2000]. The most prominent of these faults is the 150-km-long Pärvie thrust, which was active for a short period immediately after the deglaciation 9 kyr ago and produced an almost 10-m-high fault scarp [*Lagerbäck*, 1992; *Arvidsson*, 1996]. Postglacial faulting

has also been observed in Canada, where thrust as well as normal and strike-slip faulting occurred [*Adams*, 1989; *Adams et al.*, 1991]. A different example, where temporal variations in seismicity occur in the same time period as changes in the water volume of a large lake, is the Dead Sea region. Lake Lisan, the precursor of the Dead Sea, existed from 70 kyr to 15 kyr B.P. [*Kaufman et al.*, 1992] and occupied a maximum area of $\sim$2000 km^2 with an average depth of 250 m [*Bartov et al.*, 2002]. The long axis of the lake was parallel to the Dead Sea Transform Fault and associated normal faults. Paleoseismologic data derived from disturbed lake sediments and damaged cave deposits indicate infrequent clustering of earthquakes during the lifetime of Lake Lisan [*Marco et al.*, 1996; *Kagan et al.*, 2005], which experienced large variations of its lake level [*Bartov et al.*, 2002]. Future numerical modeling combining strike slip and normal faults will be needed to test whether the seismic events in the Dead Sea region are correlated with major fluctuations in the lake level.

5. Conclusions

[32] Our model results show that the rate of faulting and thus the earthquake frequency on normal faults may be controlled by large mass fluctuations on Earth's surface. In particular, the rate of faulting may be considerably increased by postglacial unloading and lithospheric rebound. This has profound implications for the inference of earthquake recurrence intervals from paleoseismologic records, because late Pleistocene/Holocene rates of faulting may not be representative on a timescale of more than 10 kyr. Many faults, for which a pronounced Holocene clustering of earthquakes has been reported, are located in regions where the volumes of lakes, glaciers or ice sheets have changed considerably in the past. Therefore slip rate variations owing to changes in surface loads may be the rule rather than an exception, in particular because regions of active faulting are generally characterized by the generation of topography and high relief, which makes them susceptible to the formation of glaciers and lakes.

[33] **Acknowledgments.** Adrian Pfiffner, Christian Schlüchter, and Ulrich Jörin are thanked for discussions on postglacial faulting and the extent of glaciers in the Swiss Alps. The Associate Editor (Steven Cohen), Bruce Bills, and an anonymous referee provided constructive comments that improved the manuscript.

References

Adams, J. (1989), Postglacial faulting in eastern Canada: Nature, origin and seismic-hazard implications, *Tectonophysics*, *163*, 323–331.

Adams, J., R. J. Wetmiller, H. S. Hasegawa, and J. Drysdale (1991), The first surface faulting from a historical intraplate earthquake in North America, *Nature*, *352*, 617–619.

Arvidsson, R. (1996), Fennoscandian earthquakes: Whole crustal rupturing related to postglacial rebound, *Science*, *274*, 744–746.

Atwood, W. W. (1909), Glaciation of the Uinta and Wasatch Mountains, *U.S. Geol. Surv. Prof. Pap.*, *61*, 96 pp.

Bartov, Y., M. Stein, Y. Enzel, A. Agnon, and Z. Reches (2002), Lake levels and sequence stratigraphy of Lake Lisan, the late Pleistocene precursor of the Dead Sea, *Quat. Res.*, *57*(1), 9–21.

Becker, A., M. Ferry, K. Monecke, M. Schnellmann, and D. Giardini (2005), Mulitarchive paleoseismic record of late Pleistocene and Holocene strong earthquakes in Switzerland, *Tectonophysics*, *400*, 153–177.

Bills, B. G., and G. M. May (1987), Constraints on lithospheric thickness and upper mantle viscosity from isostatic warping of Bonneville, Provo, and Gilbert stage shorelines, *J. Geophys. Res.*, *92*, 11,493–11,508.

Bills, B. G., D. R. Currey, and G. A. Marshall (1994), Viscosity estimates for the crust and upper mantle from patterns of lacustrine shoreline deformation in the eastern Great Basin, *J. Geophys. Res.*, *99*, 22,059–22,086.

Cohen, S. C. (1993), Does rapid change in ice loading modulate strain accumulation and release in glaciated, tectonically active regions?, *Geophys. Res. Lett.*, *20*, 2123–2126.

Coulomb, C. A. (1773), Sur une application des régles de maximis et minimis a quelques problémes de statique relatifs a l'árchitecture, *Acad. R. Sci. Mem. Math. Phys.*, *7*, 343–382.

Ellis, S., and B. Stöckhert (2004), Elevated stresses and creep rates beneath the brittle-ductile transition caused by seismic faulting in the upper crust, *J. Geophys. Res.*, *109*, B05407, doi:10.1029/2003JB002744.

Ferry, M., M. Meghraoui, B. Delouis, and D. Giardini (2005), Evidence for Holocene palaeoseismicity along the Basal-Reinach active normal fault (Switzerland): A seismic source for the 1356 earthquake in the Upper Rhine graben, *Geophys. J. Int.*, *160*, 554–572.

Fjeldskaar, W. (1994), Viscosity and thickness of the asthenosphere detected from the Fennoscandian uplift, *Earth Planet. Sci. Lett.*, *126*, 399–410.

Fjeldskaar, W., C. Lindholm, J. F. Dehls, and I. Fjeldskaar (2000), Postglacial uplift, neotectonics and seismicity in Fennoscandia, *Quat. Sci. Rev.*, *19*, 1413–1422.

Florineth, D., and C. Schlüchter (1998), Reconstructing the Last Glacial Maximum (LGM) ice surface geometry and flowlines in the central Swiss Alps, *Eclogae Geol. Helv.*, *91*(3), 391–407.

Friedrich, A., B. P. Wernicke, N. A. Niemi, R. A. Bennett, and J. L. Davis (2003), Comparison of geodetic and geologic data from the Wasatch region, Utah, and implications for the spectral character of Earth deformation at periods of 10 to 10 million years, *J. Geophys. Res., 108*(B4), 2199, doi:10.1029/2001JB000682.

Gilbert, G. K. (1890), Lake Bonneville, *U. S. Geol. Surv. Mongr.*, *1*, 438 pp.

Gillespie, R., and P. Molnar (1995), Asynchronous maximum advances of mountain and continental glaciers, *Rev. Geophys.*, *33*(3), 311–364.

Gudmundson, G. H. (1994), An order-of-magnitude estimate of the current uplift-rates in Switzerland caused by the Würm Alpine deglaciation, *Eclogae Geol. Helv.*, *87*(2), 545–557.

Hetzel, R., and A. Hampel (2005), Slip rate variations on normal faults during glacial-interglacial changes in surface loads, *Nature*, *435*, 81–84.

Hibbitt, Karlsson and Sorenson (2002), *ABAQUS/Standard User's Manual*, version 6.3, Hibbitt, Karlsson and Sorenson, Pawtucket, R. I.

Jackson, J. A. (1987), Active normal faulting and crustal extension, in *Continental Extensional Tectonics*, edited by M. P. Coward, J. F. Dewey, and P. L. Hancock, *Spec. Publ. Geol. Soc. London*, *28*, 3–17.

Jaeger, J. C., and N. G. W. Cook (1979), *Fundamentals of Rock Mechanics*, 593 pp., CRC Press, Boca Raton, Fla.

Johnston, A. C. (1987), Suppression of earthquakes by large continental ice sheets, *Nature*, *330*, 467–469.

Johnston, A. C. (1989), The effect of large ice sheets on earthquake genesis, in *Earthquakes at North-Atlantic Passive Margins: Neotectonics and Postglacial Rebound*, edited by S. Gregersen and P. W. Basham, pp. 581–599, Springer, New York.

Johnston, P., P. Wu, and K. Lambeck (1998), Dependence of horizontal stress magnitude on load dimension in glacial rebound models, *Geophys. J. Int.*, *132*, 41–60.

Kagan, E. J., A. Agnon, M. Bar-Matthews, and A. Ayalon (2005), Dating large infrequent earthquakes by damaged cave deposits, *Geology*, *33*, 4261–4264.

Kaiser, A., K. Reicherter, C. Hübscher, and D. Gajewski (2005), Variation of the present-day stress field within the north German basin: Insights from thin shell FE modeling based on residual GPS velocities, *Tectonophysics*, *397*, 55–72.

Kaufman, A., Y. Yechieli, and M. Gardosh (1992), Reevaluation of the lake sediment chronology in the Dead Sea basin, Israel, based on the ^{230}Th/^{234}U dates, *Quat. Res.*, *38*, 292–304.

Kelly, M. A., J.-F. Buonchristiani, and C. Schlüchter (2004), A reconstruction of the Last Glacial Maximum ice-surface geometry in the western Swiss Alps and contiguous Alpine regions in Italy and France, *Eclogae Geol. Helv.*, *47*, 57–75.

Klemann, V., and D. Wolf (1998), Modelling the stresses in the Fennoscandian lithosphere induced by Pleistocene glaciations, *Tectonophysics*, *294*, 291–303.

Klemann, V., and D. Wolf (1999), Implications of a ductile crustal layer for the deformation caused by the Fennoscandian ice sheet, *Geophys. J. Int.*, *139*, 216–226.

Lagerbäck, R. (1992), Dating of late Quaternary faulting in northern Sweden, *J. Geol. Soc.*, *149*, 285–291.

Lambeck, K., and J. Chappell (2001), Sea level change through the last glacial cycle, *Science*, *292*, 679–686.

Lambeck, K., C. Smither, and P. Johnston (1998), Sea-level change, glacial rebound and mantle viscosity for northern Europe, *Geophys. J. Int.*, *142*, 102–144.

Machette, M., S. F. Personius, and A. R. Nelson (1991), The Wasatch fault zone, Utah-segmentation, and history of Holocene earthquakes, *J. Struct. Geol.*, *13*, 137–149.

Madsen, D. B., and D. R. Currey (1979), Late Quaternary glacial and vegetation changes, Little Cottonwood Canyon, Wasatch Mountains, Utah, *Quat. Res.*, *12*, 254–270.

Marco, S., M. Stein, A. Agnon, and H. Ron (1996), Long-term earthquake clustering: A 50,000-year palaeoseismic record in the Dead Sea graben, *J. Geophys. Res.*, *101*, 6179–6191.

McCalpin, J. P., and S. P. Nishenko (1996), Holocene palaeoseismicity, temporal clustering, and probabilities of future large (M > 7) earthquakes on the Wasatch fault zone, Utah, *J. Geophys. Res.*, *101*, 6233–6253.

Mohr, C. O. (1900), Welche Umstände bedingen die Elastizitätsgrenze und den Bruch eines Materials?, *Z. Ver. Dtsch. Ing.*, *44*, 1524–1530, 1572–1577.

Muir-Wood, R. (2000), Deglaciation seismotectonics: A principal influence on intraplate seismogenesis at high latitudes, *Quat. Sci. Rev.*, *19*, 1399–1411.

Osborn, G., and K. Bevis (2001), Glaciation in the Great Basin of the western United States, *Quat. Sci. Rev.*, *20*, 1377–1410.

Oviatt, C. G., D. R. Currey, and D. Sack (1992), Radiocarbon chronology of Lake Bonneville, eastern Great Basin, USA, *Palaeogeogr. Palaeoclimat. Palaeoecol.*, *99*, 225–241.

Rahm, G. (1977), Eine Stauchendmoräne und andere Stauchungserscheinungen in Glazialtälern der Südvogesen, *Ber. Naturforsch. Ges. Freiburg i. Br.*, *67*, 249–253.

Rahm, G. (1987), Die Vergletscherung des Belchengebiets (Südschwarzwald) zur Würmeiszeit, *Eiszeitalter Geg.*, *37*, 31–39.

Sauber, J., and B. F. Molnia (2004), Glacier ice mass fluctuations and fault instability in tectonically active southern Alaska, *Global Planet. Change*, *42*, 279–293.

Sauber, J., G. Plafker, B. F. Molnia, and M. A. Bryant (2000), Crustal deformation associated with glacial fluctuations in the eastern Chugach Mountains, Alaska, *J. Geophys. Res.*, *105*, 8055–8077.

Schwarz, M., and A. Henk (2005), Evolution and structure of the Upper Rhine graben: Insights from three-dimensional thermomechanical modelling, *Int. J. Earth Sci.*, *94*, 732–750.

Seret, G., E. Dricot, and G. Wansard (1990), Evidence for an early glacial maximum in the French Vosges during the last glacial cycle, *Nature*, *346*, 453–456.

Shackleton, N. J. (1987), Oxygen isotopes, ice volume and sea level, *Quat. Sci. Rev.*, *6*, 183–190.

Smith, R. B., W. C. Nagy, K. A. Julander, J. J. Viveiros, C. A. Baker, and D. B. Gants (1989), Geophysical and tectonic framework of the eastern Basin and Range–Colorado Plateau–Rocky Mountains transition, *Mem. Geol. Soc. Am.*, *172*, 205–233.

Stewart, S., J. Sauber, and J. Rose (2000), Glacio-seismotectonics: Ice sheets, crustal deformation and seismicity, *Quat. Sci. Rev.*, *19*, 1367–1389.

Twiss, R. J., and E. M. Moores (1992), *Structural Geology*, 532 pp., W. H. Freeman, New York.

Walcott, R. I. (1970), Isostatic response to loading of the crust in Canada, *Can. J. Earth Sci.*, *7*, 716–729.

Watts, A. B. (2001), *Isostasy and Flexure of the Lithosphere*, 458 pp., Cambridge Univ. Press, New York.

Weijermars, R. (1997), *Principles of Rock Mechanics*, 352 pp., Alboran Sci. Publ., Amsterdam.

Wu, P., and H. S. Hasegawa (1996a), Induced stresses and fault potential in eastern Canada due to a disc load: A preliminary analysis, *Geophys. J. Int.*, *125*, 415–430.

Wu, P., and H. S. Hasegawa (1996b), Induced stresses and fault potential in eastern Canada due to a realistic load: A preliminary analysis, *Geophys. J. Int.*, *127*, 215–299.

Wu, P., and P. Johnston (2000), Can deglaciation trigger earthquakes in N. America?, *Geophys. Res. Lett.*, *27*, 1323–1326.

Wu, P., P. Johnston, and K. Lambeck (1999), Postglacial rebound and fault instability in Fennoscandia, *Geophys. J. Int.*, *139*, 657–670.

Zandt, G., S. C. Myers, and T. C. Wallace (1995), Crust and mantle structure across the Basin and Range–Colorado Plateau boundary at 37°N latitude and implications for Cenozoic extensional mechanism, *J. Geophys. Res.*, *100*(B6), 10,529–10,548.

Zienert, A. (1973), Die Würm-Vereisung und ihre Rückzugsstadien im Westteil des Hochschwarzwaldes (Teilrevision), *Z. Geomorphol.*, *17*(3), 359–366.

Zoback, M. L., et al. (1989), Global patterns of tectonic stress, *Nature*, *341*, 291–298.

A. Hampel, Institut für Geologie, Mineralogie und Geophysik, Ruhr-Universität Bochum, Universitätsstrasse 150, D-44801 Bochum, Germany.

R. Hetzel, Geologisch-Paläontologisches Institut, Universität Münster, Corrensstrasse 24, D-48149 Münster, Germany.